

Strongly entangled Quantum Spin Rings driven by Hückel rule

Manish Kumar^{1,4,†}, Deng-Yuan Li^{2,†,*}, Zhangyu Yuan^{3,†}, Ying Wang², Diego Soler-Polo¹,
Enzo Monino⁵, Libor Veis⁵, Yi-Jun Wang², Xin-Yu Zhang⁶, Can Li³, Jinfeng Jia^{3,7,9},
Pei-Nian Liu^{2,*}, Pavel Jelinek^{1,8,*}, Shiyong Wang^{3,9,*}

¹Institute of Physics, Academy of Sciences of the Czech Republic, Cukrovarnická 10, 162 00, Prague, Czech Republic

²Key Laboratory of Natural Medicines, Department of Medicinal Chemistry, China Pharmaceutical University, Nanjing 211198, China

³State Key Laboratory of Micro-nano Engineering Science, Key Laboratory of Artificial Structures and Quantum Control (Ministry of Education), School of Physics and Astronomy, Shanghai Jiao Tong University, Shanghai 200240, China

⁴Department of Condensed Matter Physics, Faculty of Mathematics and Physics, Charles University, Prague 2, CZ 12116, Czech Republic

⁵Department of Theoretical Chemistry, J. Heyrovsky Institute of Physical Chemistry, Czech Academy of Sciences, Prague 18200, Czech Republic

⁶School of Chemistry and Molecular Engineering, East China University of Science and Technology, Shanghai 200237, China

⁷Hefei National Laboratory, Hefei 230088, China

⁸Regional Centre of Advanced Technologies and Materials, Czech Advanced Technology and Research Institute (CATRIN), Palacký University Olomouc, 779 00 Olomouc, Czech Republic

⁹Tsung-Dao Lee Institute, Shanghai Jiao Tong University, Shanghai, 200240, China

[†]These authors contributed equally

*Corresponding author: dengyuanli@cpu.edu.cn, liupn@cpu.edu.cn, jelinekp@fzu.cz, shiyong.wang@sjtu.edu.cn

Abstract

Quantum spin rings represent an intriguing platform for studying unconventional magnetic order and exotic quantum phases, and they are also promising materials for emerging quantum technologies. Conventional spin systems consist of a set of weakly interacting localized spins that are well described by the Heisenberg spin models. Here, we demonstrate that strong interactions between radical centers in macrocycles of different sizes lead to fluctuations in the total number of unpaired electrons and to non-trivial antiferromagnetic order that extends beyond the Heisenberg picture. We demonstrate that the electronic structure of these spin rings is governed by the concept of $4n/4n + 2$ Hückel (anti)aromaticity for even-membered rings, whereas odd-membered rings possess a highly degenerate frustrated magnetic ground state. The strongly coupled spin rings are experimentally realized through the on-surface synthesis of π -magnetic carbon-based macrocycles, which consist of [2]triangulene units. The close correlation between the electronic structure and the Hückel aromaticity rule is revealed by scanning tunneling spectroscopy and multireference calculations. This work establishes a novel design principle employing the concept of Hückel aromaticity for quantum spin macrocycles.

The quest to construct atomically precise molecular quantum spin rings with tunable quantum properties stands at the frontier of molecular materials science¹ and also promises new materials for emerging quantum technologies². A particularly interesting aspect is the possibility to form a frustrated magnetic order with a highly degenerate ground states³⁻⁵. More broadly, the preparation of new molecular magnets with ring topology exhibiting non-trivial magnetic ordering expands the portfolio of current synthetic chemistry.

Recent breakthroughs in on-surface synthesis in ultrahigh vacuum (UHV) conditions⁶ have enabled the fabrication of exotic carbon allotropes, including cyclo[N]carbons, through tip-induced manipulation on insulating surfaces⁷⁻¹⁰. These pioneering studies have demonstrated that molecular rings containing $4n + 2$ π -electrons exhibit aromatic character, whereas $4n$ systems display anti-aromatic behavior, predictions rooted in Hückel's rule that have guided chemical intuition for nearly a century.

Series of macrocyclic polyradicaloids was synthesized with antiferromagnetically coupled π -electrons in cyclic form¹¹⁻¹³. In terms of aromaticity, particularly interesting are polyradicaloid polyaromatic hydrocarbon (PAH) macrocycles featuring a unique annulene-within-annulene (AWA) super-ring structure^{14;15}. Such AWA structures show complex π -aromaticity, where the inner and outer annulene rings may exhibit distinct aromatic character following Hückel's or Baird's rule¹⁴.

More recently, [n]triangulene units have been used as building blocks to construct low-dimensional π -magnets with unconventional electronic and magnetic properties, including linear chains¹⁶⁻¹⁹ and rings^{20;21}. In these works, the presence of well-defined localized spins arises from weak hybridization between singly occupied zero-energy modes φ_{SOMO} of triangulene units originating from the imbalance of the bipartite

lattice²². For [2]triangulene, the presence of a single φ_{SOMO} (Fig. 1a) gives rise to spin-1/2 building block. The weak coupling is caused by a particular connection through atomic sites of the bipartite lattice of [2]triangulene that do not host the radical state φ_{SOMO} (Fig. 1b, top). Consequently, spin-1/2 characters that originate from a topological zero energy mode with antiferromagnetic (AFM) coupling between neighbor spins are retained, as depicted in Fig. 1c and Fig. S1a. Consequently, the magnetic properties reflect Heisenberg’s picture, driven by local antiferromagnetic exchange interactions between adjacent well-defined spin centers rather than the global π -electron topology, thereby preventing any significant role for aromaticity.

In parallel, odd-membered π -magnetic rings, lying outside the conventional $4n/4n + 2$ aromatic classifications, have attracted growing interest due to their frustrated spin topology^{3;4}. For odd-membered AFM spin-1/2 rings, a fourfold-degenerate ground state is composed of two symmetry-related doublets. Their degenerate electronic structure provides a complementary platform where geometric frustration, rather than Hückel aromaticity alone, defines the strongly correlated ground state. In a recent study of five-membered triangulene rings^{21;23}, steric hindrance between adjacent triangulene units, imposed by a short linker, prevented the formation of the frustrated ground state. Consequently, frustrated odd-membered π -magnetic rings have so far remained largely theoretical, and an experimental platform that clearly manifests their magnetic frustrated ground states is still lacking.

Here, we introduce a design strategy that employs the concept of Hückel rules in quantum spin rings. We consider extended π -conjugated macrocycles in which spin-1/2 [2]triangulene units are specifically connected through atomic sites that host the singly occupied radical state φ_{SOMO} (Fig. 1b, bottom) via a diyne C_4 linker. This connectivity enforces strong hybridization between adjacent radical states, i.e., $\langle \varphi_{\text{SOMO}} | \varphi'_{\text{SOMO}} \rangle \neq 0$, and they hybridize to form bonding and antibonding molecular orbitals (Fig. S1c). In the dimer, strong hybridization together with electron-electron correlation leads to the open-shell singlet ground state²⁴ as shown experimentally and theoretically in Fig. S1-3. Extending this motif to rings, the strong hybridization of the radical states φ_{SOMO} within the cycle leads to delocalization of the electronic states and produces antiferromagnetic order over the entire ring (Fig. 1c). For convenience, we refer to these molecular spin rings as the Hückel- spin ring ($H\ddot{u}\text{-}SR^N$), hereinafter, where N corresponds to the number of [2]triangulene units for reasons discussed later.

The effect of the delocalization reflected in the evolution of the character of one-electron Hückel spectra of different $H\ddot{u}\text{-}SR^N$, as shown in Fig. 1e. For $H\ddot{u}\text{-}SR^4$, 28 carbon atoms (highlighted in red in Fig. 1e) form an inner carbon cycle corresponding to $4n$ π -electron count and thus to anti-aromatic character. Consequently, according to Hückel’s rules, there are two topological zero-energy modes φ_{SOMO} hosting two unpaired electrons (Fig. 1e), giving $H\ddot{u}\text{-}SR^4$ a strong diradical character. In contrast, $H\ddot{u}\text{-}SR^6$ has $N_c = 42$ carbon atoms in the inner cycle, which satisfies the $4n + 2$ aromatic rule; its one-electron spectrum therefore shows

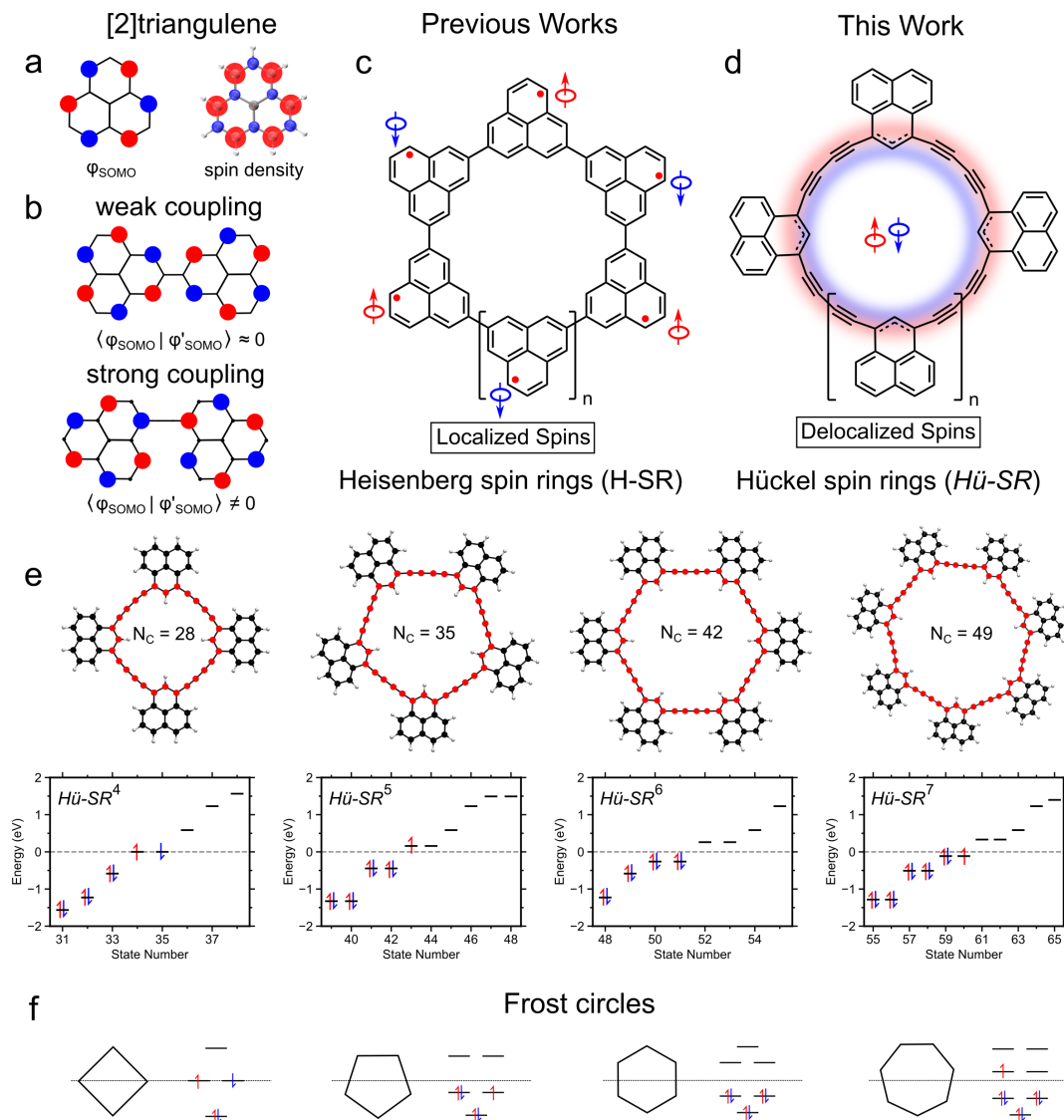


Fig. 1. Concept of Hückel spin rings. **a**, Spatial localization of the zero-energy radical mode φ_{SOMO} (left) and calculated spin density of [2]triangulene unit. **b**, Two connection motifs between two [2]triangulene units: weak coupling, where the two φ_{SOMO} do not overlap directly; and strong coupling, where the two φ_{SOMO} hybridize to form bonding and antibonding molecular orbitals. **c**, Antiferromagnetic Heisenberg rings: localized-spin nanorings made of [2]triangulene units, in which the connection through specific atomic sites results in weak hybridization. Their magnetic properties follow the Heisenberg spin model and are driven by local antiferromagnetic exchange rather than by the global π -topology. **d**, Hückel spin rings, in which [2]triangulene units are connected via polyynic C_4 linkers. This connectivity enforces strong hybridization, resulting in delocalized spins and magnetic properties governed by Hückel's $4n/4n + 2$ rules. **e**, Atomic structures of Hückel spin rings with different numbers of [2]triangulene units and their corresponding one-electron energy spectra. Carbon atoms (highlighted in red) form an inner ring whose electron count determines the $4n$ (antiaromatic) or $4n + 2$ (aromatic) character. **f**, Frost circles for the rings in (e), rationalizing the alternation of radical character with the number of [2]triangulene units.

closed-shell character, albeit with a relatively small band gap (Fig. 1e).

For odd-membered *Hü-SR*, the Hückel energy spectrum exhibits doubly degenerate frontier orbitals

φ_{SOMO} that host one ($H\ddot{u}\text{-}SR^5$) or three ($H\ddot{u}\text{-}SR^7$) electrons, respectively (Figs. 1e). For completeness, Fig. S4 shows the one-electron spectra for larger rings $H\ddot{u}\text{-}SR^{8-12}$, which reveal alternating $4n/4n + 2$ character for even-membered $H\ddot{u}\text{-}SR$ depending on the number of carbon atoms (N_c) in the inner ring. For odd-membered rings, two doubly degenerate frontier orbitals are always present and host one or three unpaired electrons. Overall, this analysis indicates that for π -magnetic $H\ddot{u}\text{-}SR$ with strongly hybridized radical states φ_{SOMO} , the electronic structure follows the Frost-circle picture (Fig. 1f) imposed by the cyclic boundary conditions. However, electron correlation plays a central role in $H\ddot{u}\text{-}SR$, so the one-electron Hückel model and Frost circles provide radical originating only from the topological zero energy modes, and multireference methods are required for a quantitative description, as discussed below.

To corroborate these results, an on-surface synthesis approach was employed to prepare the desired $H\ddot{u}\text{-}SR$. To achieve the construction of molecular spin rings with even and odd numbers [2]triangulene units, we designed and synthesized a molecular precursor with a closed shell structure, 4,6-bis(chloroethynyl)-2,3-dihydro-1H-[2]triangulene (BCE- H_3 -Tr) by solution methods (see detailed synthesis and structural characterization in the Supplementary Material). On the naphthalene ring of BCE- H_3 -Tr, two meta-chloroethynyl groups are expected to form diyne bridges on the Au(111) surface via an intermolecular dechlorination C-C coupling reaction²⁵, and 1,3-propylene ($\text{CH}_2\text{CH}_2\text{CH}_2$) can undergo STM tip-induced dehydrogenation to achieve the transformation from sp^3 to sp^2 hybridized carbon²⁶, resulting in the formation of diyne-bridged [2]triangulene polymers. As shown schematically in Fig. 2a, the molecular precursors BCE- H_3 -Tr were deposited onto a clean Au(111) surface held at 378 K under ultrahigh vacuum conditions. After annealing at 378 K for 1 h, STM measurements revealed the formation of the linear polymer chains and cyclic oligomers (Fig. S5). Subsequently, STM tip-induced dehydrogenation of cyclic oligomers yielded molecular spin rings with $N = 4$ to 13 [2]triangulene units (see Fig. S5d-g and Fig. S6). Bond-resolved nc-AFM images of representative $H\ddot{u}\text{-}SR^{4-7}$ confirm alternating [2]triangulene units and diyne bridges (Fig. 2b).

Fig. 2c shows experimental scanning tunneling spectroscopy (STS) spectra acquired for different macrocycles $H\ddot{u}\text{-}SR^4$ to $H\ddot{u}\text{-}SR^7$. The spectra exhibit distinct low-energy excitations that depend on whether the number N of [2]triangulene units is even or odd. For even-membered rings ($N = 4, 6$), symmetric step-like features were observed that are commonly attributed to inelastic tunneling processes associated with spin-flip transitions between the ground and excited states²⁷. For odd-membered macrocycles, we detect zero-bias resonances, consistent with Kondo screening of molecular spins on metal surfaces²⁸. For $H\ddot{u}\text{-}SR^7$ and larger rings, step-like features associated with spin-flip excitations are also observed. The step-like signal is not clearly resolved for $H\ddot{u}\text{-}SR^5$, which we attribute to the proximity of ionic resonances in the same energy range in the STS, hindering the detection of the spin excitation signal.

Fig. 3a (black square) summarizes the lowest spin-excitations ΔE_{01} obtained from experimental STS

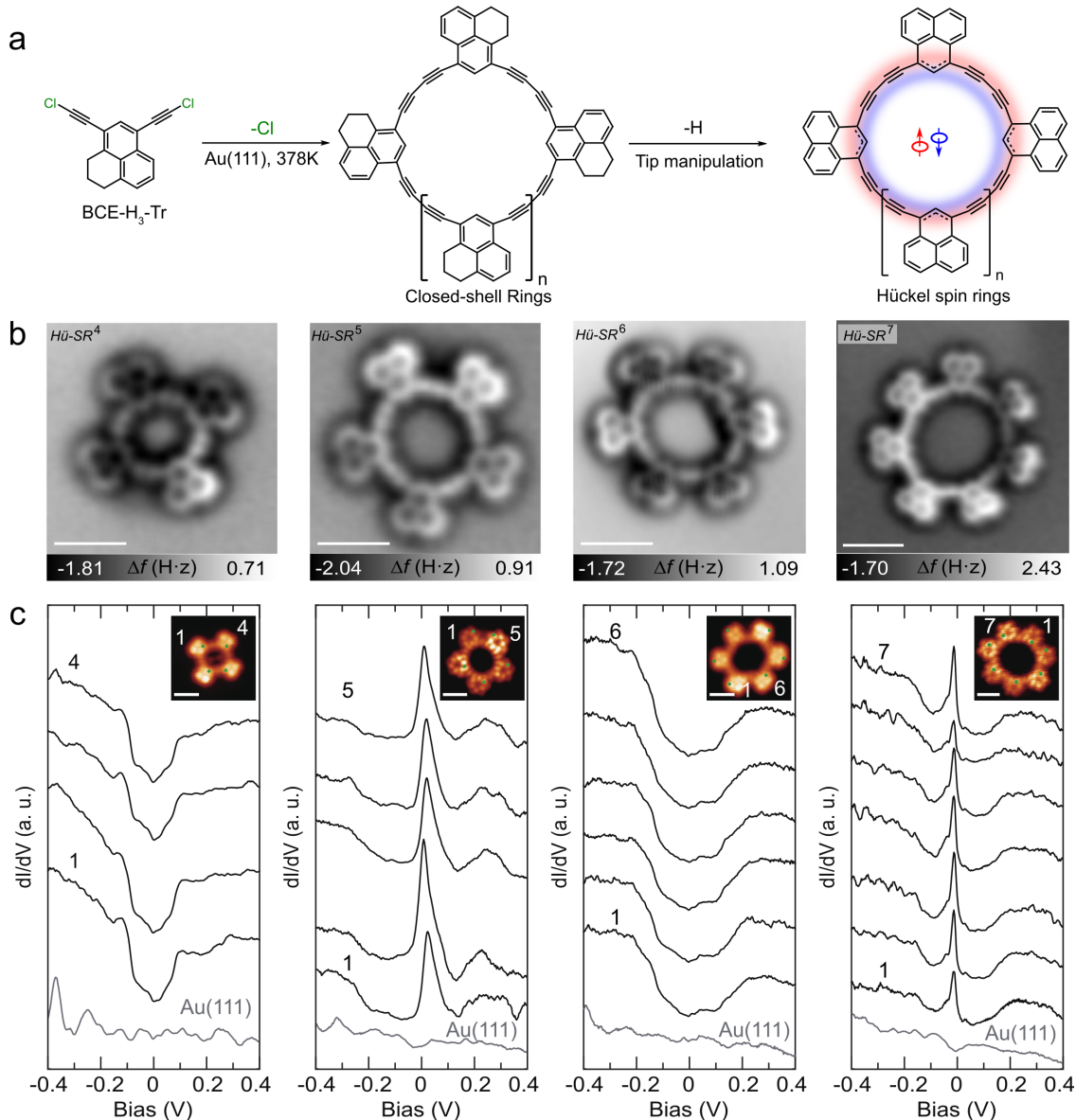


Fig. 2. Design and synthesis of molecular Hückel spin rings. **a**, Schematic illustration of the synthetic pathway, involving surface-assisted dechlorination C–C coupling followed by STM tip-induced dehydrogenation. **b**, AFM images of molecular spin rings composed of alternating [2]triangulene units and diyne bridges. Scale bar: 1 nm. **c**, STS (dI/dV) spectra of macrocycles Hü-SR⁴ to Hü-SR⁷. Even-membered rings (Hü-SR⁴ and Hü-SR⁶) display symmetric step-like features characteristic of inelastic spin-flip excitations, whereas odd-membered rings (Hü-SR⁵ and Hü-SR⁷) exhibit zero-bias resonances. Scale bar: 1 nm.

spectra for Hü-SR^N up to $N = 13$. The spin-excitation data exhibit an even-odd oscillation and, overall, a decrease with increasing N . Notably, the size dependence is not strictly monotonic as ΔE_{01} for Hü-SR⁴ is lower than that of Hü-SR⁶, in contrast to the behavior expected for a Heisenberg spin ring (blue circles).

To rationalize the experimental STS measurements and better understand the electronic structure of Hü-SR, we performed multireference complete active space configuration interaction (CASCI) calculations.

We used geometries optimized in the gas phase with density functional theory (DFT) (see Fig. S5). Whereas single-determinant DFT favours a broken-symmetry solution, multireference CASCI yields a lower energy for fully symmetric geometries, indicating the absence of a Jahn-Teller distortion in $H\ddot{u}$ - SR (see Supplementary Material).

Fig. 3a compares experimental and theoretical values of the lowest spin excitation ΔE_{01} showing very good agreement. We attribute overall difference in the absolute values of the spin excitation ΔE_{01} between the experiment and the theoretical CASCI calculations to the absence of metal surface screening in the multireference calculations, which generally reduces the value of the spin excitation²⁹. In particular, we would like to emphasize that the experimentally observed decrease of the spin excitation ΔE_{01} between $H\ddot{u}$ - SR^6 and $H\ddot{u}$ - SR^4 is well reproduced by the multireference CASCI calculations.

For even-membered $H\ddot{u}$ - SR , the calculated electronic structure shows the multireference open-shell singlet as ground state and triplet state as the first excited state (Supplementary Figs. S10–15). Importantly, the singlet-triplet excitation energy ΔE_{01} shows non-monotonic character with N , which is inherently connected to variation of (anti)aromatic character and associated one-electron Hückel spectra of $H\ddot{u}$ - SR^N . For antiaromatic $H\ddot{u}$ - SR^4 , which in one-electron picture has open-shell character with two degenerate topological zero energy modes φ_{SOMO} (Fig. 1e), CASCI(12,12) calculation gives $\Delta E_{01} = 177$ meV. Nevertheless, for aromatic $H\ddot{u}$ - SR^6 , multireference calculations give a higher singlet-triplet excitation $\Delta E_{01} = 183$ meV, in good agreement with the experimental observation. Here, the increase of ΔE_{01} is caused by the fact that Hückel energy spectra show close shell character. However, in the multireference CASCI calculations, the enhanced electron-electron correlation facilitated by a relatively small one-electron band gap^{30;31} gives rise to an open-shell singlet but with a larger ΔE_{01} compared to $H\ddot{u}$ - SR^4 . This scenario is also confirmed by the calculated radical character Y_d^i proposed by Yamaguchi et al³² using CASCI calculations (Fig. 3b, red line), which evolves non-monotonically with N number of [2]triangulene units. Namely, we observe that the radical character decreases from $H\ddot{u}$ - SR^4 to $H\ddot{u}$ - SR^6 . In general, the radical character of $H\ddot{u}$ - SR exhibits a significantly different behavior compared to the Heisenberg spin rings (blue line), whose radical character is generally higher and almost linear with the number N of [2]triangulene units. These theoretical comparisons provide direct evidence of the role of (anti)aromatic behavior on the magnetic properties of $H\ddot{u}$ - SR^N , which deviates from the traditional Heisenberg picture. Finally, $H\ddot{u}$ - SR exhibits substantially larger spin-excitation energies ΔE_{01} than previously reported Heisenberg-type spin rings, reflecting the strong hybridization of the radical states.

Figs. 3c,d compare experimental and simulated STS maps obtained from natural transition orbitals (NTO) corresponding to the singlet-triplet transition for $H\ddot{u}$ - $SR^{4,6}$. Very good agreement between experimental and simulated STS maps confirms that the step-like feature in STS is associated with the singlet-

triplet transition.

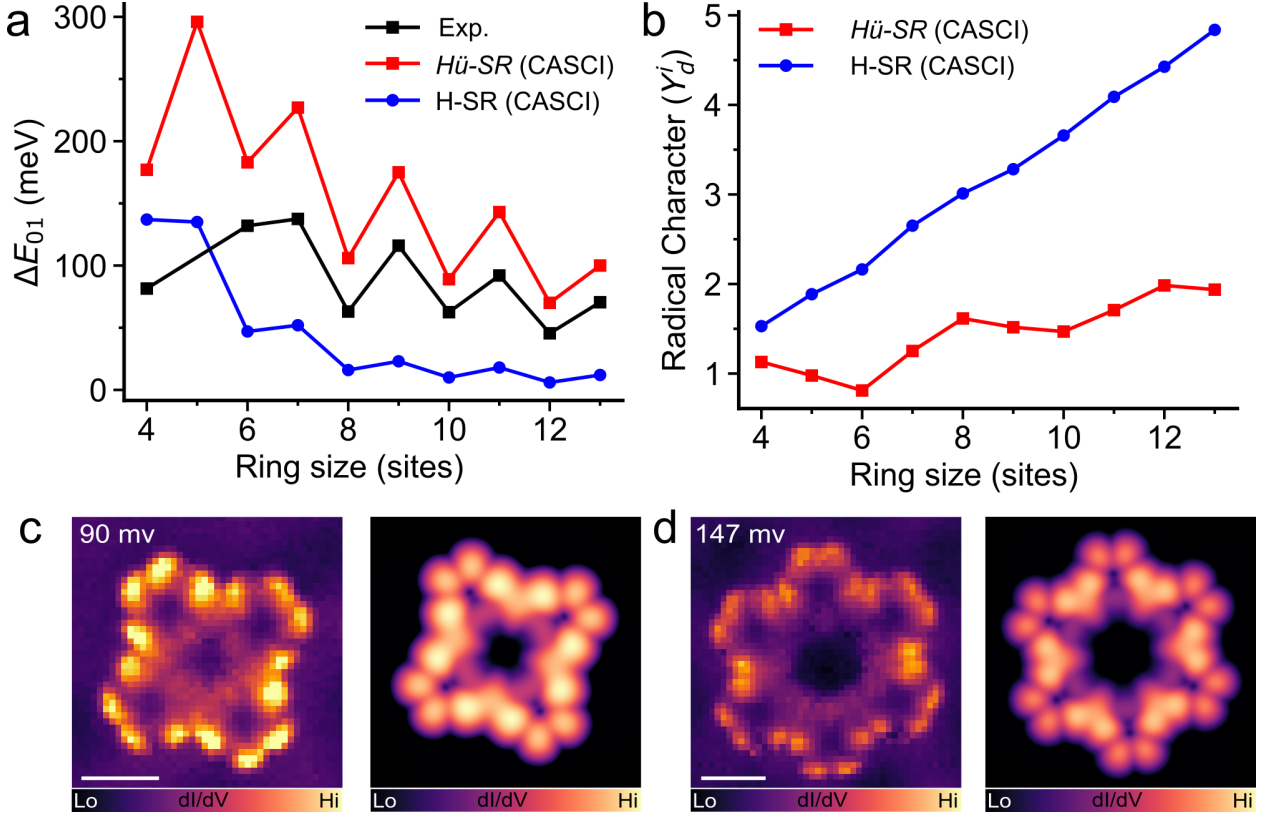


Fig. 3. Magnetic properties of molecular spin rings. **a**, Lowest spin-excitation energies ΔE_{01} as a function of ring size N obtained from experimental STS (black), CASCI calculations for $H\ddot{u}$ -SR N (red), and the Heisenberg spin ring (H-SR, blue) shown in Fig. 1c. **b**, Total radical character Y_d versus ring size N for $H\ddot{u}$ -SR (red) and the Heisenberg spin ring (H-SR, blue). **c**, Comparison of experimental constant-current STS maps acquired at 90 meV with simulated STS maps computed from CASCI NTOs for the singlet–triplet excitation of $H\ddot{u}$ -SR 4 . **d**, Comparison of experimental constant-current STS maps acquired at 147 meV with simulated STS maps computed from CASCI NTOs for the singlet–triplet excitation of $H\ddot{u}$ -SR 6 . Scale bars: 1 nm.

For odd-membered $H\ddot{u}$ -SR, STS reveals the presence of zero-energy resonances tentatively associated with Kondo screening (Fig. 2c). Constant-current STS maps acquired near the Fermi level show that the zero-energy signal is distributed homogeneously over the entire $H\ddot{u}$ -SR (Figs. 4a,b). According to CASCI(11,11) calculations, the ground state of odd-membered $H\ddot{u}$ -SR consists of two doubly degenerate doublet states $\Psi_{0,1}^D$ with strong multireference character (see Supplementary Figs. S17–S23), arising from frustrated antiferromagnetic interactions between spin-1/2 radicals (Fig. 4). The first excited states form a manifold of doubly-degenerate quartet states $\Psi_{2,3}^Q$.

To rationalize the zero-energy resonances in terms of Kondo screening, we computed Kondo orbitals³³ corresponding to Kondo screening of two degenerate doublet ground states $\Psi_{0,1}^D$ by conduction electrons of the metal substrate (Fig. 4d). Importantly, these two Kondo orbitals exhibit distinct spatial localization

distributed over different parts of the $H\ddot{u}$ - SR . To recover the experimentally observed spatially homogeneous distribution of the STS maps, simulated STS maps therefore need to include the contribution from Kondo orbitals associated with both doublets. Excellent agreement between experimental and simulated STS maps (Figs. 4a,b) supports the assignment to Kondo screening. Moreover, the delocalized Kondo signal over the entire molecule points out the frustrated magnetic structure of the synthesized odd-membered $H\ddot{u}$ - SR as a consequence of the degenerate doublet ground state, as schematically depicted in Fig. 4c. In addition, Fig. S7 and Supplementary Fig. S22 show the natural transition orbitals for the allowed spin excitations between the degenerate doublet ground states and the excited quartet states. The experimentally observed homogeneous STS map at energies corresponding to the step-like features (e.g., $H\ddot{u}$ - SR^7) is reproduced only when all symmetry-allowed $\Psi_{0,1}^D \rightarrow \Psi_{2,3}^Q$ transitions are taken into account (Fig. 4c). These results provide evidence for frustrated magnetic order arising from a degenerate ground state^{3,4}.

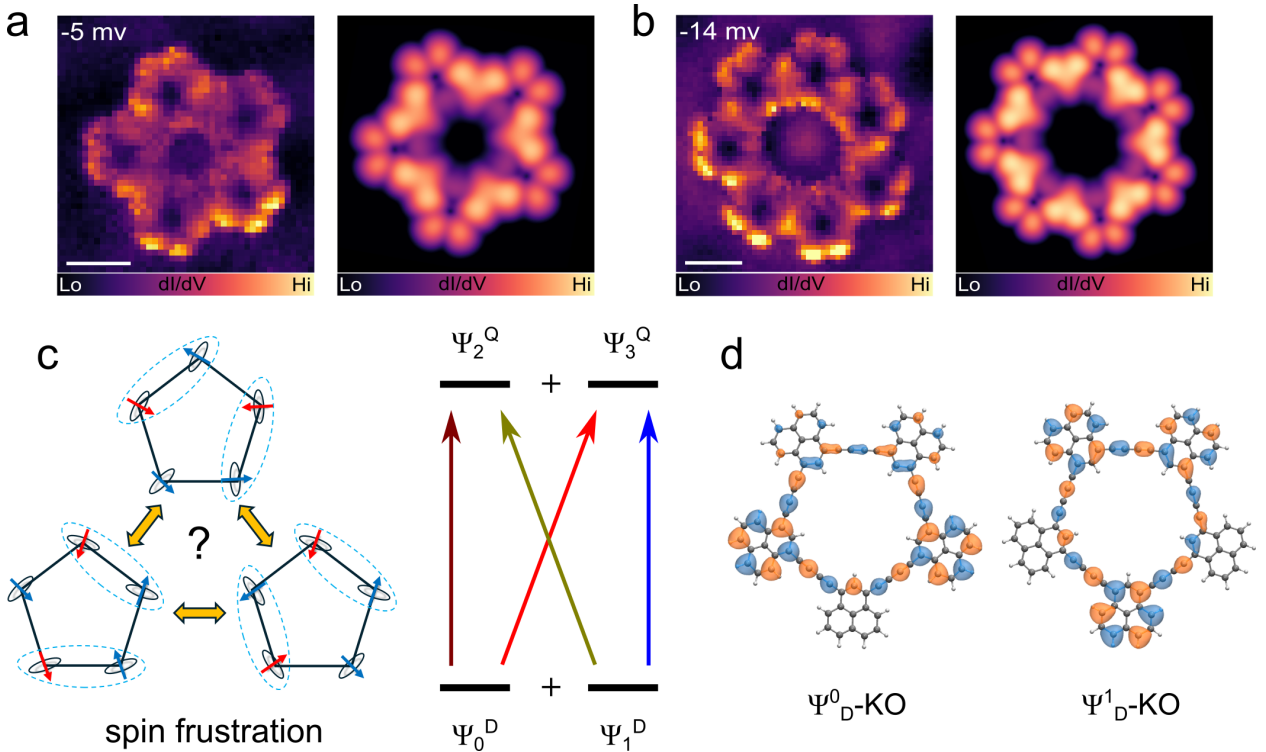


Fig. 4. Frustrated magnetic order of odd-membered $H\ddot{u}$ - SR . **a**, Comparison of experimental constant-current STS maps acquired at -5 meV with simulated constant-height STS maps computed from CASCI Kondo orbitals associated with Kondo screening of the degenerate doublet ground states $\Psi_{0,1}^D$ of $H\ddot{u}$ - SR^5 on a metal surface. **b**, Comparison of experimental constant-current STS maps acquired at -14 meV with simulated constant-height STS maps computed from CASCI Kondo orbitals associated with Kondo screening of the degenerate doublet ground states $\Psi_{0,1}^D$ of $H\ddot{u}$ - SR^7 on a metal surface. **c**, Schematic representation of frustrated spin order in $H\ddot{u}$ - SR^5 , showing competing local magnetic configurations with entangled singlets (dashed ovals, right). Energy-level scheme for odd-membered $H\ddot{u}$ - SR doubly degenerate doublet ground state $\Psi_{0,1}^D$ and first excited quartet states $\Psi_{2,3}^Q$, indicating magnetic frustration. **d**, Calculated CASCI Kondo orbitals associated with screening of the two degenerate doublet states $\Psi_{0,1}^D$ by the metallic substrate, highlighting their distinct spatial distributions. Scale bars: 1 nm.

Conclusion

These results demonstrate that aromaticity can be leveraged as a design principle to control quantum states in π -magnetic carbon-based spin rings, enabling the creation of cyclic systems whose magnetic properties arise from long-range electronic correlations rather than local exchange. This bottom-up approach enables the design of diverse magnetic states with tunable spin excitations and spin frustration. This approach provides a foundation for engineering π -magnetic carbon-based molecular materials with strongly entangled electronic structures, with potential application in spintronics and quantum information technologies.

Methods

Precursor synthesis. Molecular precursor (BCE-H₃-Tr) was synthesized from 4,6-dibromo-1H-phenalen-1-one by solution methods (see the detailed procedure and data in Supplementary Information).

Sample preparation and STM/nc-AFM measurements. A commercially available low-temperature Unisoku Joule-Thomson scanning probe microscope (1.2 K) and Liquid-helium free scanning probe microscope from CASAcme (4.3 K) operated at ultrahigh vacuum (3×10^{-10} mbar) was used for all sample preparation and characterization. The Au(111) single crystals were cleaned using repeated cycles of Ar⁺ sputtering and subsequent annealing to 950 K to obtain atomically flat terraces. The cleanliness of the crystals was checked by scanning with the STM before molecular deposition. Precursor BCE-H₃-Tr were thermally deposited on the clean Au(111) surface at 378 K for 1 hour. Precursor BCE-H₃-Tr was evaporated on the surface from a quartz crucible and the sublimation temperature was approximately 333 K. Then, the sample was transferred to a cryogenic scanner at 1.2 K for characterization. Carbon monoxide molecules were dosed onto the cold sample around 9 K (1×10^{-8} mbar, 1 minute). A lock-in amplifier (531 Hz, 0.1-1 mV modulation) has been used to obtain dI/dV spectra. The STM and STS measurements were taken at 1.2 K, and the data were processed with the WSxM software. The bond-resolved nc-AFM images were acquired with Unisoku Joule-Thomson system operated at approximately 1.2 K. To achieve ultra-high spatial resolution, CO molecule was picked up from the Au(111) surface to the apex of a tungsten tip. A quartz tuning fork with a resonant frequency of 26 kHz has been used in nc-AFM measurements. The sensor was operated in frequency modulation mode with a constant oscillation amplitude of 0.3 Å. AFM measurements were performed in constant-height mode with Bias = 1 mV. STS mappings were acquired using Liquid-helium free scanning probe microscope.

CASCI calculations. Molecular geometries were optimized in the high-spin state using density functional theory (DFT) as implemented in FHI-aims³⁴. The PBE0 exchange–correlation functional³⁵ was

used, and van der Waals interactions were included via the Tkatchenko—Scheffler method³⁶. Given the open-shell, multiradical character of the studied molecules, complete active space configuration interaction (CASCI) calculations were performed to accurately describe the wavefunctions and electronic energies³⁷. One- and two-electron integrals were constructed in the basis of molecular orbitals around the Fermi energy using the ORCA quantum chemistry package³⁸, with orbitals obtained from restricted open-shell Kohn-Sham (ROKS) calculations. Active spaces of CAS(11,11) (odd-electron systems) and CAS(12,12) (even-electron systems) were employed, except for *Hü-SR*¹³, for which CAS(13,13) was used. The number of unpaired electrons was estimated from natural-orbital occupations obtained by diagonalizing the one-particle density matrix of the ground-state CASCI wavefunction.

Kondo orbitals (KO). Kondo orbitals were obtained by diagonalizing the Hamiltonian derived from the multi-channel Anderson model, which incorporates the many-body multiplet structure of molecules obtained from the CASCI neutral ground state and virtual charge states, as described in Ref.³³.

Natural transition orbitals (NTOs). Natural transition orbitals (NTOs)³⁹ were computed for the spin-flip process between the ground state and the first excited state to capture the spatial variation of the dI/dV maps corresponding to IETS spin excitation maps.

Simulated nc-AFM and dI/dV images were obtained using the probe-particle code^{40;41} with optimized geometries from total-energy DFT calculations.

Radical character evaluation. Radical character was evaluated using the approach proposed by Yamaguchi *et al.*³². Successive pairs of natural orbitals, consisting of the highest occupied natural orbital (HONO $-i$) and the lowest unoccupied natural orbital (LUNO $+i$), were considered. For each pair, a diradical coefficient $Y_d^{(i)}$ is defined as

$$Y_d^{(i)} = 1 - \frac{2T_i}{1 + T_i^2}, \tag{1}$$

where

$$T_i = \frac{n_{\text{HONO}-i} - n_{\text{LUNO}+i}}{2}. \tag{2}$$

Here, $n_{\text{HONO}-i}$ and $n_{\text{LUNO}+i}$ are the occupation numbers of the corresponding natural orbitals, and i labels successive orbital pairs.

The total radical character is estimated by summing contributions from multiple orbital pairs,

$$Y_d^{\text{total}} = \sum_i Y_d^{(i)}, \tag{3}$$

which provides an effective measure of polyradical character when multiple orbital pairs exhibit substantial fractional occupation. For odd-membered rings, 0.5 is added to Y_d^{total} to account for the SOMO contribution

(one natural orbital with occupation 1.0).

Acknowledgments

We acknowledge the support from NSFC(22325203, 92577203, 22272050), GACR 25-17866X and the Czech-NanoLab Research Infrastructure supported by MEYS CR (LM2023051). We also acknowledge the financial support from the TERAFFIT project (CZ.02.01.01/00/22_008/0004594) and Shanghai Jiao Tong University 2030 Initiative for financial support.

Competing Interests

The authors declare no competing interests.

Author Contributions

S.W., P.J. and D.Y.L. conceived and supervised the project. P.J. and M.K. provided theoretical concept of Hückel spint ring. M.K., D.S.P., E.M., L.V. and P.J. performed theoretical calculations and underlying interpretation. Z.Y., C.L. and Y.W. performed the STM/STS and nc-AFM measurements under the supervision of J.J., D.Y.L. and S.W.. Y.J.W. and X.Y.Z. synthesized the precursor molecules under the supervision of D.Y.L. and P.N.L.. P.J., M.K., D.Y.L. and S.W. wrote the manuscript with the input of all authors. All authors have given approval to the final version of the manuscript.

References

- [1] Zhang, Y., Fu, B., Li, N., Lu, J. & Cai, J. Advancements in π -magnetism and precision engineering of carbon-based nanostructures. *Chemistry – A European Journal* **30** (2024). URL <http://dx.doi.org/10.1002/chem.202402765>.
- [2] Troiani, F. *et al.* Molecular engineering of antiferromagnetic rings for quantum computation. *Physical Review Letters* **94** (2005). URL <http://dx.doi.org/10.1103/PhysRevLett.94.207208>.
- [3] Kahn, O. Competing spin interactions and degenerate frustration for discrete molecular species. *Chemical Physics Letters* **265**, 109–114 (1997). URL [http://dx.doi.org/10.1016/S0009-2614\(96\)01424-8](http://dx.doi.org/10.1016/S0009-2614(96)01424-8).
- [4] Schnack, J. Effects of frustration on magnetic molecules: a survey from olivier kahn until today. *Dalton Transactions* **39**, 4677 (2010). URL <http://dx.doi.org/10.1039/B925358K>.
- [5] Baker, M. L. *et al.* A classification of spin frustration in molecular magnets from a physical study of large odd-numbered-metal, odd electron rings. *Proceedings of the National Academy of Sciences* **109**, 19113–19118 (2012). URL <http://dx.doi.org/10.1073/pnas.1213127109>.
- [6] Clair, S. & de Oteyza, D. G. Controlling a chemical coupling reaction on a surface: Tools and strategies for on-surface synthesis. *Chemical Reviews* **119**, 4717–4776 (2019). URL <http://dx.doi.org/10.1021/acs.chemrev.8b00601>.
- [7] Kaiser, K. *et al.* An sp-hybridized molecular carbon allotrope, cyclo[18]carbon. *Science* **365**, 1299–1301 (2019). URL <http://dx.doi.org/10.1126/science.aay1914>.
- [8] Albrecht, F. *et al.* The odd-number cyclo[13]carbon and its dimer, cyclo[26]carbon. *Science* **384**, 677–682 (2024). URL <http://dx.doi.org/10.1126/science.ado1399>.
- [9] Sun, L. *et al.* On-surface synthesis of aromatic cyclo[10]carbon and cyclo[14]carbon. *Nature* **623**, 972–976 (2023). URL <http://dx.doi.org/10.1038/s41586-023-06741-x>.
- [10] Gao, Y. *et al.* On-surface synthesis of a doubly anti-aromatic carbon allotrope. *Nature* **623**, 977–981 (2023). URL <http://dx.doi.org/10.1038/s41586-023-06566-8>.
- [11] Lu, X. *et al.* Stable 3, 6-linked fluorenyl radical oligomers with intramolecular antiferromagnetic coupling and polyradical characters. *Journal of the American Chemical Society* **138**, 13048–13058 (2016). URL <http://dx.doi.org/10.1021/jacs.6b08138>.

- [12] Das, S. *et al.* Fully fused quinoidal/aromatic carbazole macrocycles with poly-radical characters. *Journal of the American Chemical Society* **138**, 7782–7790 (2016). URL <http://dx.doi.org/10.1021/jacs.6b04539>.
- [13] Prajapati, B. *et al.* An open-shell coronoid with hybrid chichibabin–schlenk conjugation. *Angewandte Chemie International Edition* **60**, 22496–22504 (2021).
- [14] Liu, C., Ni, Y., Lu, X., Li, G. & Wu, J. Global aromaticity in macrocyclic polyradicaloids: Hückel’s rule or baird’s rule? *Accounts of Chemical Research* **52**, 2309–2321 (2019). URL <http://dx.doi.org/10.1021/acs.accounts.9b00257>.
- [15] Villalobos, F. *et al.* Globally aromatic odd-electron π -magnetic macrocycle. *Chem* **11**, 102316 (2025). URL <http://dx.doi.org/10.1016/j.chempr.2024.09.015>.
- [16] Yuan, Z. *et al.* Fractional spinon quasiparticles in open-shell triangulene spin-1/2 chains. *Journal of the American Chemical Society* **147**, 5004–5013 (2025).
- [17] Mishra, S. *et al.* Observation of fractional edge excitations in nanographene spin chains. *Nature* **598**, 287–292 (2021). URL <http://dx.doi.org/10.1038/s41586-021-03842-3>.
- [18] Zhao, Y. *et al.* Quantum nanomagnets in on-surface metal-free porphyrin chains. *Nature Chemistry* **15**, 53–60 (2022). URL <http://dx.doi.org/10.1038/s41557-022-01061-5>.
- [19] Zhao, C. *et al.* Spin excitations in nanographene-based antiferromagnetic spin-1/2 heisenberg chains. *Nature Materials* **24**, 722–727 (2025). URL <http://dx.doi.org/10.1038/s41563-025-02166-1>.
- [20] Hieulle, J. *et al.* On-surface synthesis and collective spin excitations of a triangulene-based nanostar. *Angewandte Chemie International Edition* **60**, 25224–25229 (2021). URL <http://dx.doi.org/10.1002/anie.202108301>.
- [21] Li, D. *et al.* Frustration-induced many-body degeneracy in spin- 1/2 molecular quantum rings. *Journal of the American Chemical Society* **147**, 26208–26217 (2025).
- [22] Ovchinnikov, A. A. Multiplicity of the ground state of large alternant organic molecules with conjugated bonds: (do organic ferromagnetics exist?). *Theoretica Chimica Acta* **47**, 297–304 (1978). URL <http://dx.doi.org/10.1007/BF00549259>.
- [23] Li, C. *et al.* Quantum spin-1/2 rings built from [2]triangulene molecular units (2026). URL <https://arxiv.org/abs/2602.11593>.

- [24] Turco, E. *et al.* Multiconfigurational ground state of a diradicaloid characterized at the atomic scale. *Journal of the American Chemical Society* **147**, 39616–39622 (2025). URL <http://dx.doi.org/10.1021/jacs.5c13039>.
- [25] Shu, C.-H. *et al.* Atomic-scale visualization of stepwise growth mechanism of metal-alkynyl networks on surfaces. *Journal of the American Chemical Society* **142**, 16579–16586 (2020).
- [26] Li, C. *et al.* Programmable higher-order topological phases in open-shell metal–organic frameworks. *Journal of the American Chemical Society* (2025).
- [27] Hirjibehedin, C. F. *et al.* Large magnetic anisotropy of a single atomic spin embedded in a surface molecular network. *Science* **317**, 1199–1203 (2007). URL <http://dx.doi.org/10.1126/science.1146110>.
- [28] Hewson, A. C. *The Kondo Problem to Heavy Fermions* (Cambridge University Press, 1993). URL <http://dx.doi.org/10.1017/CB09780511470752>.
- [29] Zuzak, R. *et al.* On-surface synthesis and determination of the open-shell singlet ground state of tridecacene. *Angew. Chem. Int. Ed.* **63**, e202317091 (2024).
- [30] Biswas, K. *et al.* Steering large magnetic exchange coupling in nanographenes near the closed-shell to open-shell transition. *Journal of the American Chemical Society* **145**, 2968–2974 (2023). URL <http://dx.doi.org/10.1021/jacs.2c11431>.
- [31] Song, S. *et al.* Highly entangled polyradical nanographene with coexisting strong correlation and topological frustration. *Nature Chemistry* **16**, 938–944 (2024). URL <http://dx.doi.org/10.1038/s41557-024-01453-9>.
- [32] Yamaguchi, K., Takahara, Y., Fueno, T. & Houk, K. Extended hartree-fock (ehf) theory of chemical reactions: Iii. projected møller-plesset (pmp) perturbation wavefunctions for transition structures of organic reactions. *Theoretica chimica acta* **73**, 337–364 (1988).
- [33] Calvo-Fernández, A. *et al.* Theoretical model for multiorbital kondo screening in strongly correlated molecules with several unpaired electrons. *Phys. Rev. B* **110**, 165113 (2024).
- [34] Blum, V. *et al.* Ab initio molecular simulations with numeric atom-centered orbitals. *Comput. Phys. Commun.* **180**, 2175–2196 (2009).
- [35] Adamo, C. & Barone, V. Toward reliable density functional methods without adjustable parameters: The pbe0 model. *J. Chem. Phys.* **110**, 6158–6170 (1999).

- [36] Tkatchenko, A., DiStasio, R. A., Car, R. & Scheffler, M. Accurate and efficient method for many-body van der waals interactions. *Phys. Rev. Lett.* **108**, 236402 (2012). URL <http://dx.doi.org/10.1103/PhysRevLett.108.236402>.
- [37] Kumar, M. *et al.* Multireference theory of scanning tunneling spectroscopy beyond one-electron molecular orbitals: Can we image molecular orbitals? *Journal of the American Chemical Society* **147**, 24993–25003 (2025). URL <http://dx.doi.org/10.1021/jacs.5c08166>.
- [38] Neese, F. The orca program system. *Wiley Interdisciplinary Reviews: Computational Molecular Science* **2**, 73–78 (2012).
- [39] Martin, R. L. Natural transition orbitals. *J. Chem. Phys.* **118**, 4775–4777 (2003).
- [40] Hapala, P. *et al.* Mechanism of high-resolution stm/afm imaging with functionalized tips. *Phys. Rev. B* **90**, 085421 (2014). URL <http://dx.doi.org/10.1103/PhysRevB.90.085421>.
- [41] Krejčí, O., Hapala, P., Ondráček, M. & Jelínek, P. Principles and simulations of high-resolution stm imaging with a flexible tip apex. *Phys. Rev. B* **95**, 045407 (2017). URL <http://dx.doi.org/10.1103/PhysRevB.95.045407>.

SM

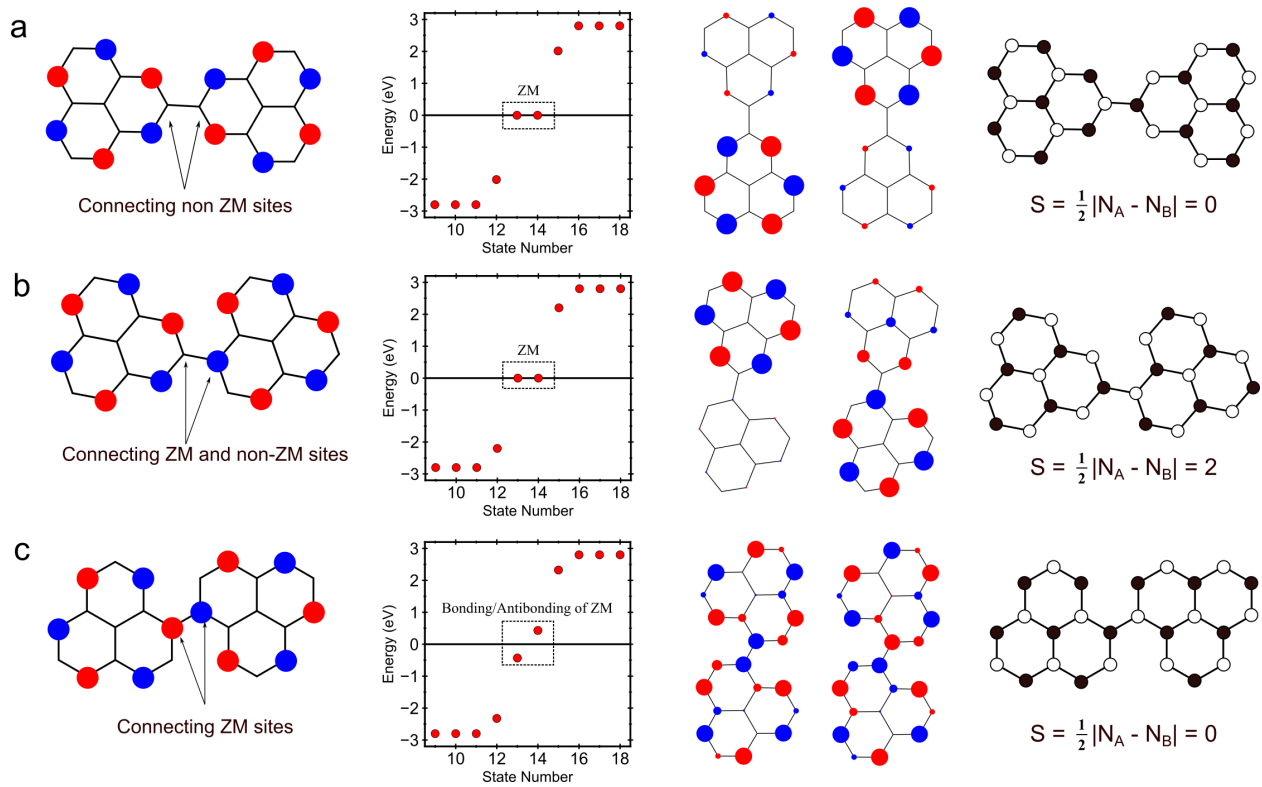


Fig. S1 | Hückel spectra for different connections in a [2]triangulene dimer. Three distinct connection motifs between two [2]triangulene units, together with their corresponding Hückel spectra (two orbitals around zero energy) and sublattice imbalance: **a**, connection between non-zero-mode (non-ZM) sites, **b**, connection between zero-mode (ZM) sites, and **c**, connection between a zero-mode (ZM) site and a non-ZM site.

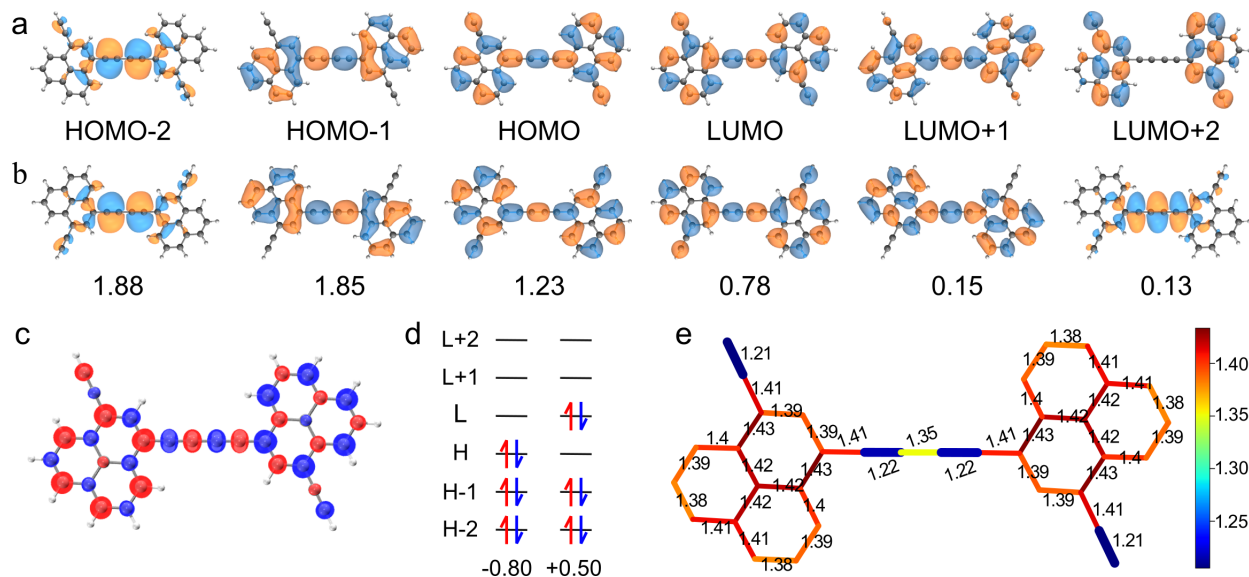


Fig. S2 | Electronic structure of a [2]triangulene dimer. **a**, Frontier DFT-PBE orbitals used for the DMRG calculation. **b**, Natural orbitals and their occupations obtained from DMRG. **c**, Isosurface of the spin density. **d**, Multireference wavefunction of the ground state. **e**, Bond lengths of the phenalene dimer are shown as a color map.

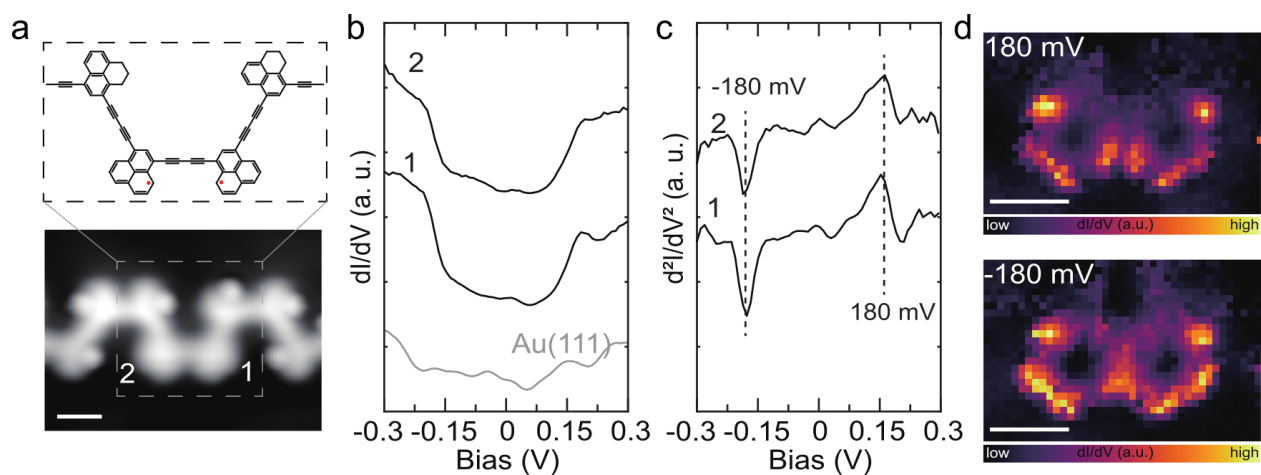


Fig. S3 | Spin excitation of a spin-1/2 dimer embedded in a closed-shell long chain. **a**, Chemical structure and STM images (300 mV, 10 pA) of a chain containing a spin-1/2 dimer; **b**, dI/dV and **c**, d^2I/dV^2 spectra acquired on the activated spin sites; and **d**, STS maps acquired at 180 meV and -180 meV. Scale bar: 1 nm.

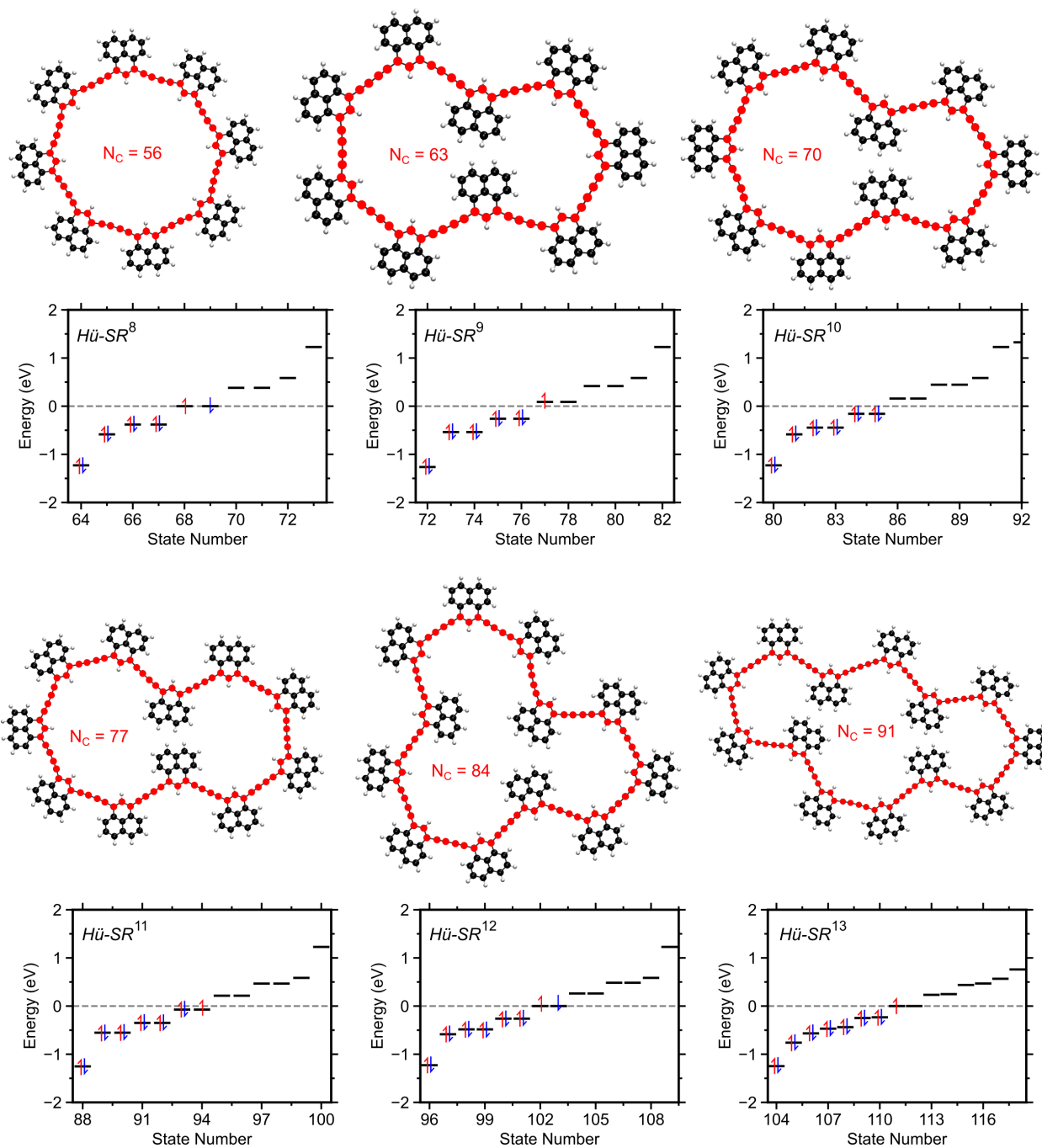


Fig. S4 | One-electron Hückel energy spectra for spin rings in which [2]triangulene units are bridged by polyynic C_4 linkers ($H\ddot{u}\text{-}SR^8$ to $H\ddot{u}\text{-}SR^{13}$).

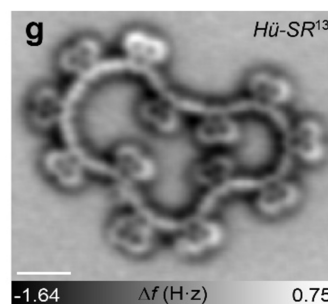
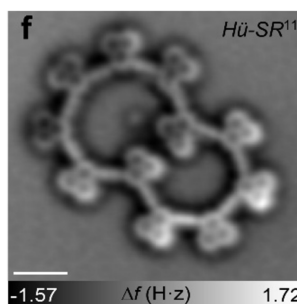
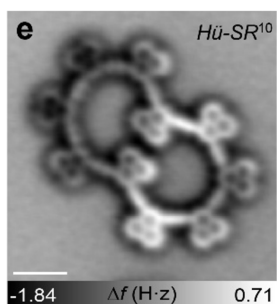
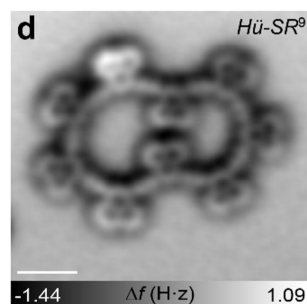
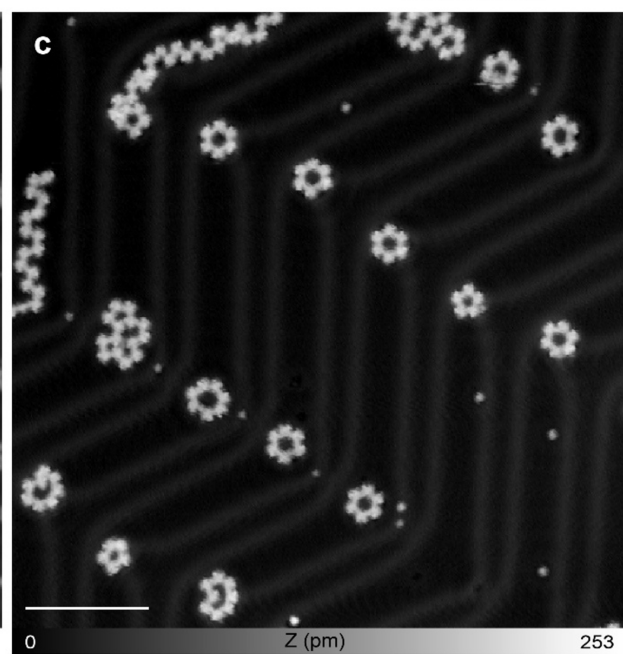
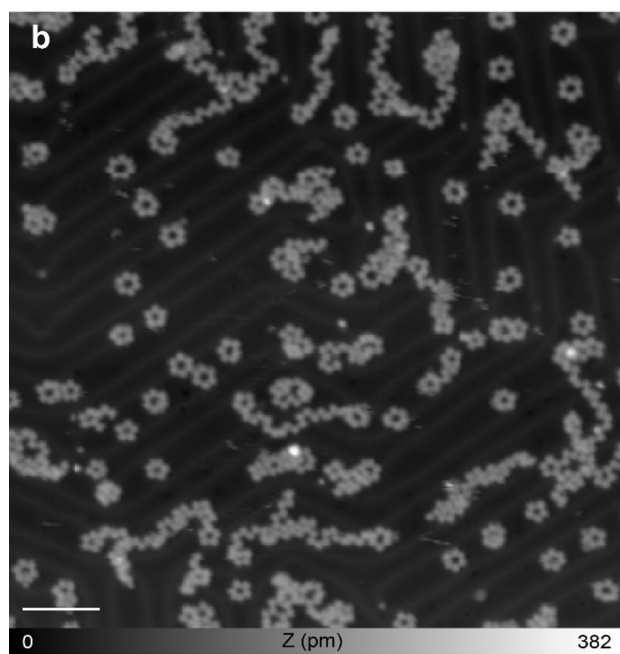
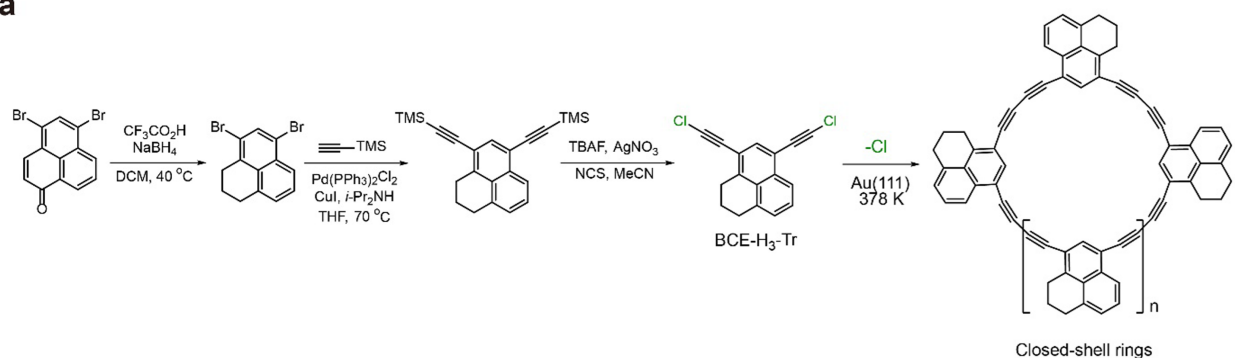
a

Fig. S5 | Synthesis of molecular rings. **a**, Synthesis scheme combining solution-phase chemistry and on-surface synthesis. **b,c**, Large-scale and zoomed-in STM images of closed-shell rings formed by depositing BCE-H₃-Tr on Au(111) and annealing at 378 K for 1 h (setpoints: $I = 10$ pA and $V_{\text{bias}} = 1$ V in **b**; $I = 10$ pA and $V_{\text{bias}} = 200$ mV in **c**; scale bars: 10 nm). **d-g**, nc-AFM images of larger Hückel spin rings ($H\ddot{u}$ -SR⁹, $H\ddot{u}$ -SR¹⁰, $H\ddot{u}$ -SR¹¹, and $H\ddot{u}$ -SR¹³) (setpoint: $V_{\text{bias}} = 1$ mV; scale bar: 1 nm).

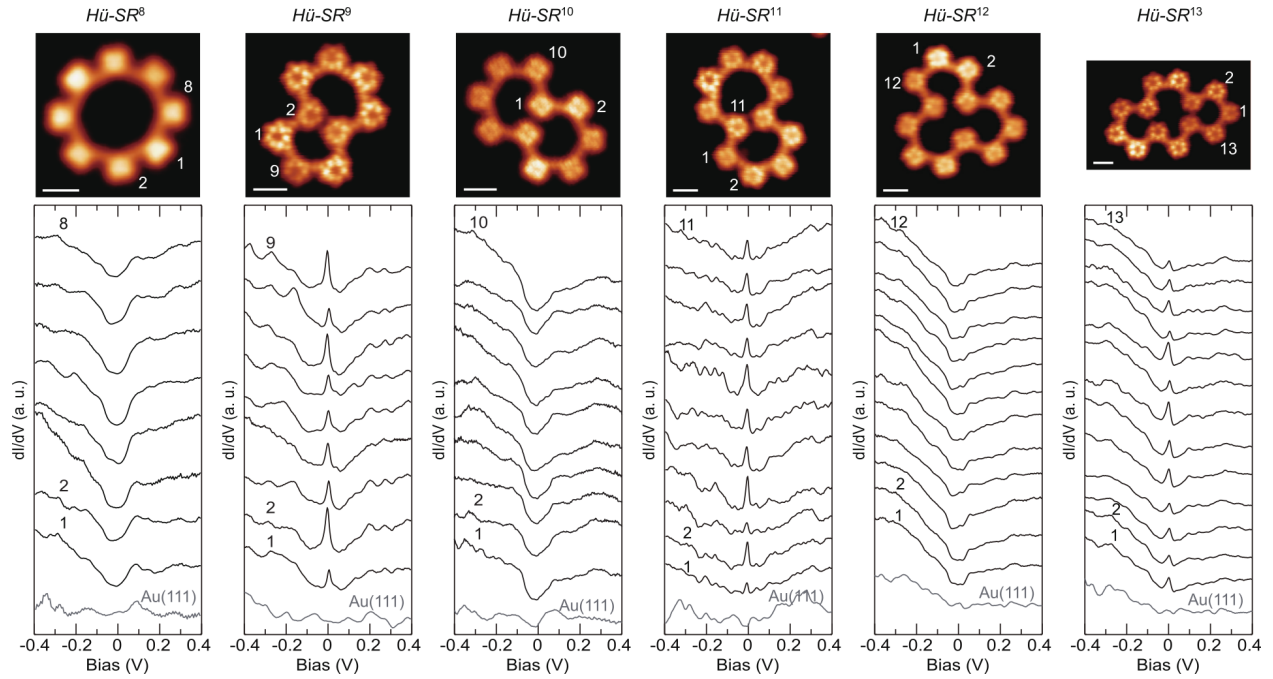


Fig. S6 | Characterization of larger molecular Hückel spin rings. Constant-height current images of $H\ddot{u}$ -SR⁸, $H\ddot{u}$ -SR⁹, $H\ddot{u}$ -SR¹⁰, $H\ddot{u}$ -SR¹¹, $H\ddot{u}$ -SR¹² and $H\ddot{u}$ -SR¹³, together with the corresponding dI/dV spectra acquired on the activated spin sites (setpoints: $V_{\text{bias}} = 10$ mV for $H\ddot{u}$ -SR⁸, $H\ddot{u}$ -SR⁹, $H\ddot{u}$ -SR¹¹ and $H\ddot{u}$ -SR¹³; $V_{\text{bias}} = 80$ mV for $H\ddot{u}$ -SR¹⁰; $V_{\text{bias}} = 140$ mV for $H\ddot{u}$ -SR¹²; scale bar: 1 nm).

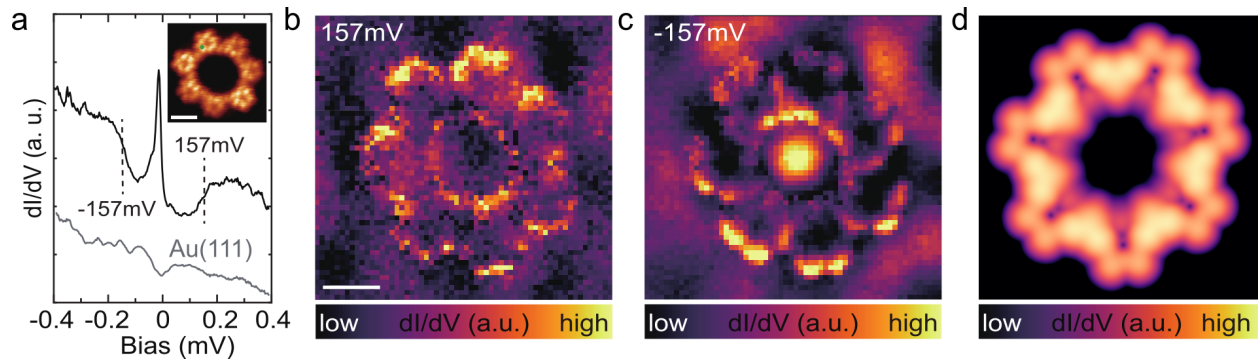


Fig. S7 | Spin excitation of $H\ddot{u}$ -SR⁷. **a**, dI/dV spectra of a $H\ddot{u}$ -SR⁷ (inset: constant-height current image, Bias = 10 mV) and **b,c**, the corresponding STS maps acquired at 157 mV and -157 mV, respectively. **d**, Simulated STS maps computed from CASCI NTOs of $H\ddot{u}$ -SR⁷. Scale bars: 1 nm.